Article

Sequential 90° Rotation of Dual-Polarized Antenna Elements in Linear Phased Arrays with Improved Cross-Polarization Level for Airborne Synthetic Aperture Radar Applications

Diego Lorente [1],*, Markus Limbach [1], Bernd Gabler [1], Héctor Esteban [2] and Vicente E. Boria [2]

1   German Aerospace Center, Microwaves and Radar Institute, SAR-Technology, 82234 Weßling, Germany; markus.limbach@dlr.de (M.L.); bernd.gabler@dlr.de (B.G.)
2   Instituto de Telecomunicaciones y Aplicaciones Multimedia, Universitat Politècnica de València, 46022 Valencia, Spain; hesteban@dcom.upv.es (H.E.); vboria@dcom.upv.es (V.E.B.)
*   Correspondence: diego.lorentecatalan@dlr.de; Tel.: +49-8153-28-2703

Abstract: In this work, a novel rotation approach for the antenna elements of a linear phased array is presented. The proposed method improves by up to 14 dB the cross-polarization level within the main beam by performing a sequential 90° rotation of the identical array elements, and achieving measured cross-polarization suppressions of 40 dB. This configuration is validated by means of simulation and measurements of a manufactured linear array of five dual-polarized cavity-box aperture coupled stacked patch antennas operating in L-Band, and considering both uniform amplitude and phase distribution and beamforming with amplitude tapering. The analysis is further extended by applying and comparing the proposed design with the 180° rotation and non-rotation topologies. This technique is expected to be used for the next generation L-Band Airborne Synthetic Aperture Radar Sensor of the German Aerospace Center (DLR).

Keywords: cross-polarization improvement; dual polarized aperture coupled stacked patch antenna; sequential element rotation; linear array; airborne SAR system

1. Introduction

Synthetic Aperture Radar (SAR) has become nowadays one of the most important fields of remote sensing. Due to the penetration of the radar waves, it becomes a versatile technique for acquisition of information, weather independence, and it delivers complementary data to optical systems. As an active radar sensor with its own target illumination, it allows day and night operational capability.

SAR provides high-resolution imaging whose geometric resolution can be independent of the acquisition distance. By means of exploiting the information given by the physical properties of the electromagnetic waves such as frequency, polarization, amplitude or phase, SAR systems offer high quality imaging data, covering a wide range of remote sensing applications. It is used for terrain topography, providing urban mapping and digital elevation models [1], oceanography, agriculture, traffic control [2] and ship detection [3], as well as for environment studies including deforestation [4], glacier and disasters monitoring, among many others. Its broad scope of research has greatly aroused the interest of the scientific community, and it has expanded its use for defense and commercial purposes.

Especially advantageous are the applications of SAR for lower frequencies [5,6] such as P-Band (216–450 MHz) or L-Band (1–2 GHz) [7]. Due to the penetrating nature of electromagnetic waves at higher wavelengths and by means of interferometry, SAR becomes an interesting way to monitor forest density and estimate forest height by using tomography [8], as well as to perform geology and glaciology studies for the measurement of snow, ice layer thicknesses and soil moisture. Furthermore, SAR polarimetry allows the use of

polarization diversity in order to identify different scattering mechanisms, enhancing this way the retrieval of information [9].

As a remote sensing system, SAR sensors are typically on board flying platforms like satellites or aircraft depending on the application itself, which leads to different coverage areas and image resolutions. Well-known SAR spaceborne missions are BIOMASS, Sentinel, TerraSAR-X and TanDEM-X, which is an add-on of the TerraSAR-X system that allows the generation of global digital elevation model data of the Earth with an unprecedent accuracy [10]. The Microwaves and Radar Institute of the German Aerospace Center (DLR) has led the development and implementation of these two spaceborne missions, TerraSAR-X and TanDEM-X. Its research work in the field of remote sensing by means of Synthetic Aperture Radar is widely known.

For the increasing demand of SAR applications and in order to support future spaceborne systems, airborne SAR provides an essential scope of research [11]. As a more flexible system, it is employed by the DLR in order to study signal processing concepts, to experiment with innovative techniques and methods, and to develop and test new components and hardware.

The German Aerospace Center operates the so-called F-SAR, an enhanced airborne multi-frequency SAR system [12]. In order to take advantage of the aforementioned capabilities of SAR imaging at lower frequency bands, a new dual-polarized phased array antenna system in L-Band for the next generation DLR airborne SAR sensor is required, which becomes also relevant for upcoming spaceborne SAR missions [13].

Due to the space limitations on the aircraft, not only a solution that fulfills the electrical and airworthiness requirements is needed, but also a high degree of compaction has to be achieved, in order to exploit the restricted available area on the airplane [14,15]. This leads to a careful selection of the implementation technology and innovative configurations for the antenna design [16,17]. As a phased array system and in order to enhance its radiation properties, some design considerations have to be made to reduce the spacing between the array elements, and at the same time minimize the antenna interactions.

Typically, the reduction of such antenna interactions involves methods to mitigate the coupling between array elements or to improve the cross-polarization level. The last one plays a key role in the performance of SAR systems that makes use of the polarization diversity to take advantage of the retrieved information of the scattered signals. Some previous research has been made and different techniques have been proposed in order to reduce the cross-polarization level. An extended approach is splitting a planar array into subarrays of 2 × 2 elements according to a rotation pattern based on the image theory arrangement, which also minimizes the side lobe level [18]. This method has been widely used in a broad range of applications [19–21]. A further analysis extends this approach by considering the inter-element coupling [22]. Some other techniques improve the cross-polarization level by rotating the antenna elements in reflectarray applications [23], or combining the 180° rotation of the antenna structure along with a 180° alternate feeding based on the overlapping of different multipolar moments [24]. Further rotation topologies such as the sequential rotation is typically used for arrays of circular polarized antennas, as it leads to an improvement of the axial ratio bandwidth or the polarization purity [25–29]. Generally, the majority of cross-polarization suppression techniques start from the decomposition of planar arrays into subarrays, and a very few applications consider linear arrays. In [30], a 90° sequential rotation technique is implemented in a circularly polarized linear array of circular patches. Later, this analysis is extended by considering the scanning properties of linear phased arrays [31]. However, this approach is simplified as the radiation effect of higher order modes is neglected and no real geometrical 90° sequential rotation is applied. To the best of the authors' knowledge, no similar 90° sequential rotation approach, as presented in this work, was applied before, not only by performing the presented rotation topology in linear array applications, but also by considering identical fed dual polarized antenna elements. In this manuscript, a novel approach to perform a 90° sequential rotation of the same identical dual polarized cavity backed aperture coupled patch antenna elements of

a linear array, for airborne SAR applications, is presented. This technique improves the cross-polarization level within the main antenna beam of up to 14 dB in comparison with the standard array arrangement, providing cross-polarization suppression values above 40 dB.

This work is structured as follows. First of all, the scope of the antenna system according to the required airborne SAR sensor requirements is presented. Later, the design of a cavity backed dual-polarized antenna element is introduced, whose compaction allows for achieving a high degree of integration and thus to maximize the number of the antenna elements. This design will be validated by means of measurements of a manufactured prototype. Later, three different configurations of a linear array composed of five identical antenna elements are constructed and measured. Each configuration that corresponds to a different rotation pattern of the array elements is analyzed when applying a uniform phase and amplitude distribution, and beamforming case with triangular amplitude tapering. Finally, these results are examined and the improvement of the cross-polarization level within the antenna main beam when performing a 90° sequential rotation is discussed.

2. Airborne SAR System Requirements

A new L-Band antenna system is required for the next generation airborne SAR sensor of the German Aerospace Center. To fulfill the system requirements, a dual polarized antenna operating in L-Band with a center frequency f_0 = 1.325 GHz and a bandwidth of 150 MHz is needed. The antenna system is a planar phased array of 5 × 8 elements with side-looking configuration by means of beamforming in elevation. The final antenna will be mounted on the DLR research aircraft Do-228 as it is shown in Figure 1.

Figure 1. F-SAR Antenna carrier.

This new design exploits the restricted available space on the antenna carrier by maximizing the number of the array elements in comparison with previous sensors [12], thus enhancing the radiation properties of the antenna and achieving a better radiation pattern shaping. The new design allows an implementation of up to 66% more antenna elements than the previous L-Band airborne system, due to the extremely compact implementation of the single element, which is based on a cavity-box stacked microstrip patch with aperture coupling feeding.

3. Antenna Single Element

Due to its conformability, integration and low cost, the antenna unit is implemented in planar technology by means of a microstrip patch as a radiating element [32]. The dual-polarization characteristic of the antenna leads to the use of a quadratic patch.

Due to the resonant nature of the microstrip patch and its narrow-band nature, a bandwidth enhancement technique by using a stacked dual patch configuration is applied, in order to achieve the required antenna bandwidth of 150 MHz specified by the SAR sensor requirements. The aperture coupling feeding technique [33] allows an independent implementation of the radiation and feeding part of the antenna, becoming a versatile method to accomplish the dual polarization excitation.

The aforementioned design considerations lead to a multi-layer structure as it can be seen in Figure 2. The design steps of the antenna element are explained in detail next. The electromagnetic analysis and optimization process of the structure were performed using HFSS, a High Frequency Simulation software tool, part of the Ansys Electromagnetics Desktop environment.
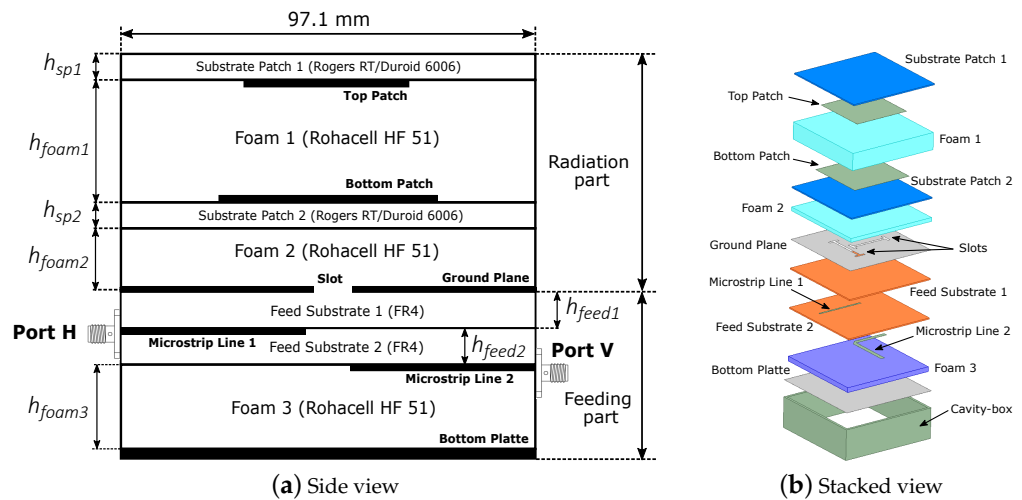

Figure 2. Antenna multilayer structure.

3.1. Bandwidth Enhancement: Dual Stacked Patch Configuration

As a resonant structure, microstrip patch antennas typically provide a narrow bandwidth (3–4%). In order to overcome this issue and to fulfill the desired system bandwidth of 150 MHz (15%), a bandwidth enhancement technique has to be applied. It is well-known that the use of substrates with a lower dielectric permittivities, such as foam layers, provides greater antenna bandwidths. In addition, the use of electrically thick substrates along with the aperture coupled feeding allows for increasing the bandwidth. However, this may also lead to a reduction of the electromagnetic coupling between the feeding slot and the microstrip patch. Thus, further methods to attain a greater broadband performance are considered [34]. The dual stacked patch configuration involves the use of two patches with different sizes, thus resonating at slightly different frequencies. This way, and together with the use of foam layers, antenna bandwidths of up to 20–30% can be achieved [35].

This stacked patch arrangement leads to a geometrical structure composed of four layers that becomes the radiating part of the antenna. Two microstrip patches (top and bottom) are implemented on a substrate Rogers RT/Duroid 6006 ($\varepsilon_r = 6.15$, $\tan \delta = 0.0019$) and thicknesses h_{sp1}, h_{sp2}, to reduce the patch size. The top patch is placed below the superstrate as it serves as a protective top layer or antenna radome. Two additional foam layers (Rohacell HF 51) with thicknesses h_{foam1} and h_{foam2} are used respectively to enhance the bandwidth and to assure a good coupling between the feeding slot and the lower patch.

The multi-layer structure of the antenna is depicted in Figure 2. The geometrical and electrical parameters of each layer are displayed in Table 1. The overall height of the antenna is 32.1 mm.

Table 1. Antenna layer properties.

Name	Substrate	ε_r	Thickness
Substrate Patch 1	Rogers RT/Duroid 6006	6.15	$h_{sp1} = 1.27$ mm
Foam 1	Rohacell HF 51	1.06	$h_{foam1} = 18$ mm
Substrate Patch 1	Rogers RT/Duroid 6006	6.15	$h_{sp2} = 1.27$ mm
Foam 2	Rohacell HF 51	1.06	$h_{foam2} = 4$ mm
Feed Substrate 1	FR4 Epoxy	4.4	$h_{feed1} = 1.27$ mm
Feed Substrate 2	FR4 Epoxy	4.4	$h_{feed2} = 1.27$ mm
Foam 3	Rohacell HF 51	1.06	$h_{foam3} = 5$ mm

3.2. Aperture Coupling Feeding

The antenna feeding is performed by means of a coupling aperture or slot that is etched on the ground plane. The bottom patch is electromagnetically coupled by this aperture slot, which at the same time is fed by a microstrip line that is placed below the ground plane. A side view of this feeding topology can be seen in Figure 2. This excitation technique allows for an independent design of the radiation and the feeding parts of the antenna. The electrical properties of each feeding layer are shown in Table 1.

The desired dual-polarization operation of the antenna requires the use of two orthogonal slots in order to excite the corresponding polarization. The H-shape smooths the field distribution at the slot edges, thus improving the coupling between the slot and the bottom patch [36]. Each slot is shifted with a small offset in order to maximize the port isolation (S_{21}), and it is fed by its respective microstrip line. Each line is placed on different FR4 substrate heights to reduce the coupling between both polarizations. The width of both lines is set to yield an impedance of 50 Ω. Figure 3 shows the spatial disposition of the slots and the feeding lines. The corresponding geometrical values are displayed in Table 2.

From now and on, the horizontal polarization (H) is excited by the slot 1 and its corresponding line 1. The same assumption is made with the vertical polarization (V) fed by the slot 2 and line 2. According to this reference, the electrical field of the horizontal polarization is along the *x*-axis and along *y* for the vertical polarization. The bending of the line 2 is done in order to place the two antenna connectors on opposite sides for further mechanical purposes.

(**a**) Feeding configuration

(**b**) Manufactured prototype (view of connector H)
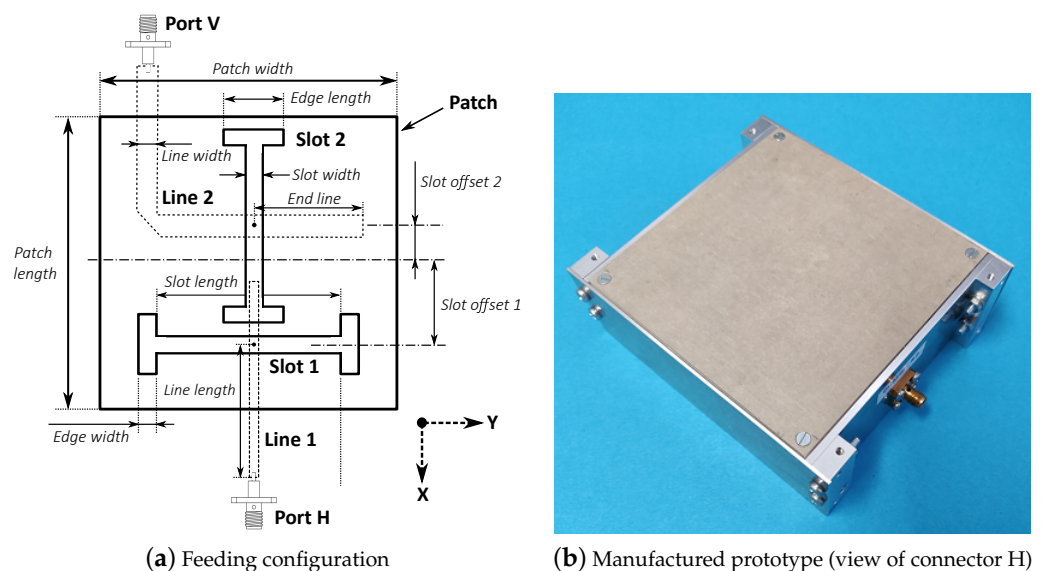
Figure 3. Antenna feeding layout and constructed prototype.

Table 2. Antenna geometrical values.

|			
Top patch length	59.6 mm	Bottom patch length	65.6 mm
Top patch width	58.8 mm	Bottom patch length	63.8 mm
End Line 1 length	18.5 mm	End Line 2 length	28.5 mm
Line 1 length	25.95 mm	Line 2 length	52.3 mm
Line 1 width	1.85 mm	Line 2 width	4.15 mm
Slot 1 length	40 mm	Slot 2 length	37 mm
Slot 1 width	2.5 mm	Slot 2 width	2.5 mm
Edge 1 length	11 mm	Edge 2 length	11 mm
Edge 1 width	2.5 mm	Edge 2 width	2.5 mm
Slot offset 1	17 mm	Slot offset 2	10 mm

3.3. Cavity-Box

The multi-layer antenna structure is enclosed within four electric walls in a cavity-box configuration. The inclusion of these walls interrupts the propagation of surface waves, which become relevant in structures composed of several layers with different dielectric permittivities. This way, the coupling between antenna elements is reduced and a higher degree of integration can be achieved, thus maximizing the density of antenna elements.

The resonant nature of the cavity leads to a bandwidth reduction due to its high quality factor. Considering this cavity-box configuration, the proposed antenna design provides a bandwidth of 150 MHz (around 15%), which still fulfills the bandwidth requirements according to the desired SAR sensor specifications.

3.4. Manufactured Prototype

The presented antenna was manufactured and measured. A picture of the fabricated prototype can be seen in Figure 3. The antenna construction requires a correct assembly in order to assure the electrical continuity between the ground plane and the walls. This construction model also allows an easy interconnection of several antennas by means of intermediate blocks in order to build the later array.

The measured S-Parameters are depicted in Figure 4. Port 1 and 2 excite the horizontal and vertical polarization, respectively. The measurement shows an excellent agreement with the simulation. It can be seen that both polarizations achieve a return loss level below –10 dB within the bandwidth of 150 MHz. The center frequency of operation is slightly shifted (around 3%) towards lower frequencies, due to fabrication and construction tolerances. The port isolation S_{21} between both polarizations is greater than 30 dB at the center frequency of operation.
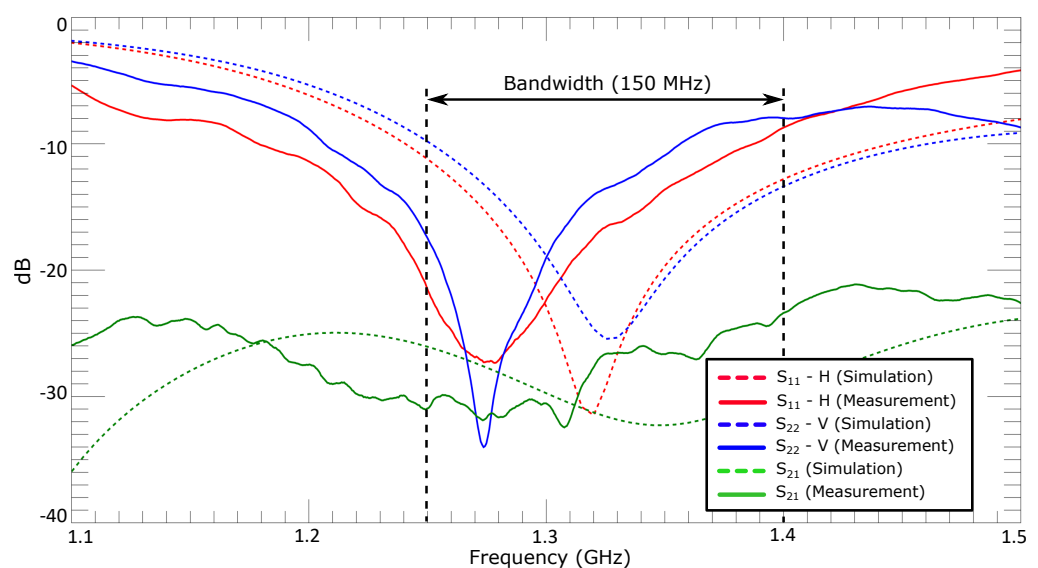
Figure 4. Simulated and measured S-parameters.

The radiation pattern of the antenna is measured at the Compact Test Range facilities of the German Aerospace Center [37]. The measured pattern meets the predicted results very well. A comparison between simulation and measurement for the two polarizations is shown in Figure 5. The measured antenna gain, 6.1 dB and 6 dB for the horizontal and vertical polarization, respectively, differs approximately 0.3 dB from the simulation. The simulated efficiency of the antenna is 90%.

(**a**) Horizontal polarization (**b**) Vertical polarization
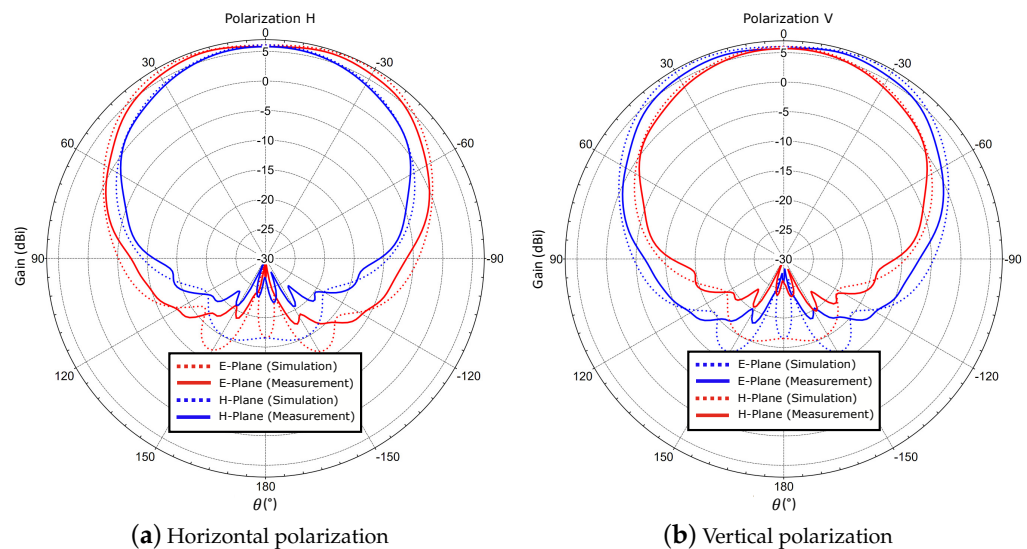
Figure 5. Simulated and measured radiation pattern of the single element @ f_0 = 1.325 GHz.

4. Antenna Array

The proposed design is extended to build a linear antenna array of five elements. The electrical performance of such configuration plays a key role in the operation of the antenna system, since it shapes the antenna radiation pattern in elevation by means of beamforming and amplitude tapering. Thus, this design stage not only allows for studying the feasibility of the proposed solution, but it also paves the way for the implementation of the final planar array of 5×8 elements.

According to the airborne SAR sensor requirements, a side-looking configuration of the antenna radiation pattern in elevation is desired. Due to the strong power echoes of the reflected signals in nadir, the projection of the aircraft flight path, a minimum of the antenna pattern in such angular direction, is required. In addition, a sidelobe level better than 20 dB is mandatory.

Since SAR polarimetry applications make use of the polarization diversity in order to exploit the information of the scattered signals, the cross-polarization level of the antenna determines an important parameter of the system performance and its reduction becomes a relevant design aspect. Some examples to improve the cross-polarization by means of different rotation schemes are found in [19–22]. However, these techniques are based on the composition of planar arrays out of 2×2 subarrays and using the image theory arrangement. In this work, a novel approach of a sequential 90° rotation of the antenna elements in linear array applications is presented.

Next, three array configurations of five elements are built and measured. Each geometrical arrangement corresponds to a different rotation topology of the antenna elements: non-rotation, sequential rotation of 180° and 90°. The performance of each configuration, in terms of co-polar and cross-polarization level, will be compared and discussed. An accurate analysis of the cross-polarization performance of the array leads to consider scenarios with antenna beam steering. Therefore, the scope of this study covers two cases for each configuration: broadside radiation and beamforming along with amplitude tapering, which can be considered as a potential SAR application.

Array design considerations

- The spacing between the antenna elements is chosen to be 0.6λ, calculated at the center frequency of operation f_0. Due to its compact implementation, an inter-element spacing of up to 0.48λ can be also considered if a higher degree of integration is desired [6]. However, for this work, a greater distance between antenna elements has to be used due to mechanical reasons, since the geometrical 90° rotation of the elements limits the access of the antenna feeding connectors.
- Each antenna is manufactured separately, and it disposes its own independent feeding; therefore, no integrated feeding network for the array is required. This allows a more flexible control of the array feeding, since two measurement scenarios with different amplitude and phase distribution are analyzed.
- The array is built along the y-axis. The same coordinate system for the array as shown in Figure 3 is considered.
- The antenna feeding ports (H_1–H_5, V_1–V_5) correspond to the antenna element numeration (1–5), starting from the left.
- The measurement setup is performed using a 1:6 power divider, model ZB6PD-17-S of Mini-Circuits [38], in order to feed the array elements. In addition, the triangular amplitude tapering is implemented by means of 3 dB and 10 dB attenuators, namely models 18AH-03 and 18AH-10, respectively, from API Inmet. Both power splitters and attenuators are not considered within the calibration.
- The phase control of each antenna element is adjusted with self-manufactured cables with the corresponding electrical length. All the cables dispose of comparable lengths in order to assure a similar phase variation within the desired frequency range.
- All the measurements are carried out with a rectangular aluminum plate (50.1 × 104.2 cm) that is attached to the array, as it is shown in Figure 6. This allows for fixing the structure under testing on top of the positioner tower of the Compact Test Range.
- The simulated and measured results are presented for the center frequency of operation 1.325 GHz.
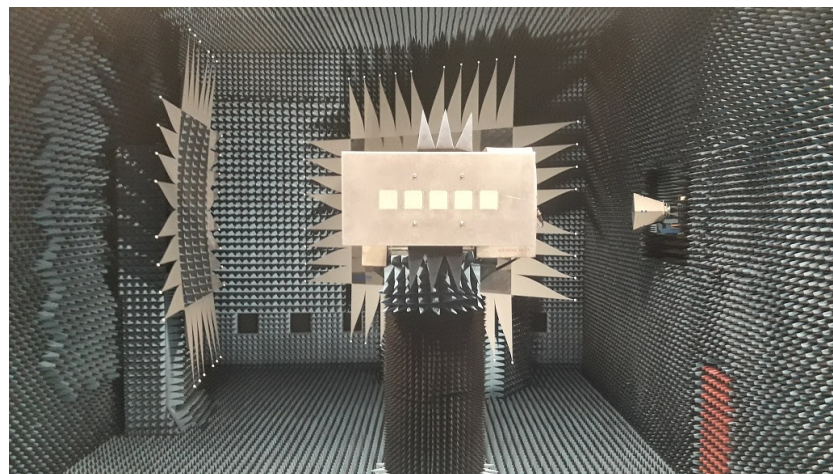
Figure 6. Picture of the antenna array in the DLR's Compact Test Range.

4.1. Normal Array

The first configuration to be analyzed corresponds to the standard case of the linear array arrangement, where all the antennas are identically aligned. This standard configuration will be identified as a normal array, and it is considered as a reference case for later comparisons. The geometrical arrangement of this configuration is depicted in Figure 7. Each antenna is interconnected by means of intermediate aluminum blocks that provide an interelement spacing of 0.6λ. The element numeration starts from the left. All the connectors that feed each polarization (H_x, V_x) are placed along the same side of the array.
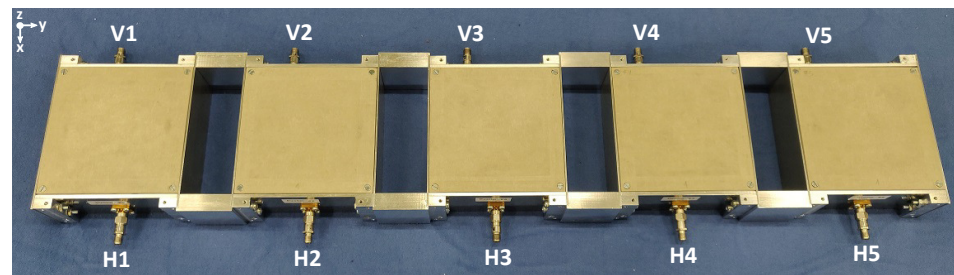
Figure 7. Manufactured normal array.

4.1.1. Uniform Amplitude and Phase Distribution

For this case, each element is fed with equal power level and phase, thus achieving a broadside radiation. The same phase value is guaranteed by means of self-manufactured cables with identical electrical length. Figure 8 shows a comparison between simulation and measurement of the co-polar patterns for both polarizations. Co-polar and cross-polar patterns for $\varphi = 90°$ are depicted in Figure 9. The measured gain is 11.1 dB and 11.7 dB for the horizontal and vertical polarization, respectively. It differs 1.7 dB from the simulated values, since the power divider used to obtain a uniform amplitude distribution for each antenna element and the cable losses are not considered within the calibration process. This includes the insertion losses related to the power divider and the inherent power losses given by the unused output of the power divider that is matched with a 50 Ω load. Precisely, due to the slight phase and amplitude unbalance at the outputs of the power divider [38], the pattern at $\varphi = 90°$ is marginally assymetric, being more visible for the vertical polarization. However, it can be seen that the measurements agree very well with the simulated values.
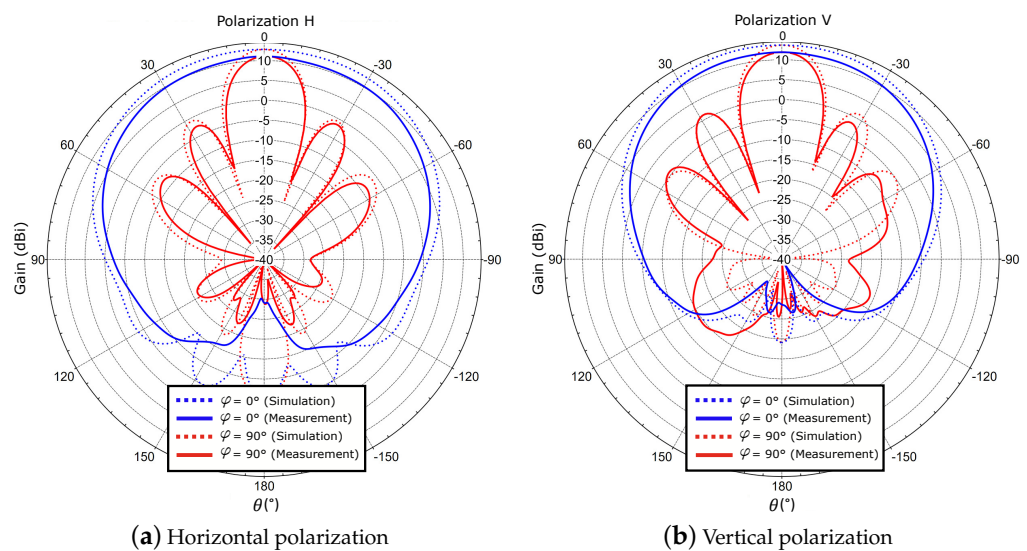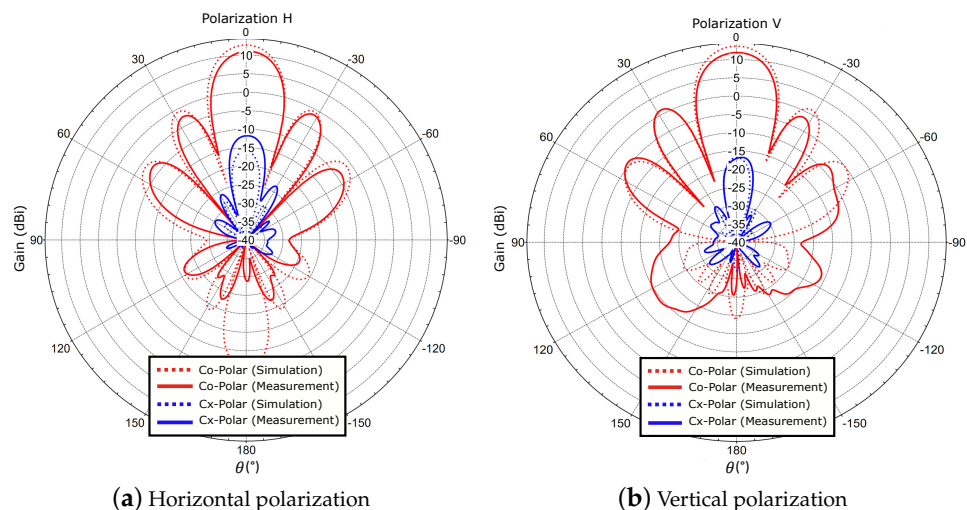

(**a**) Horizontal polarization

(**b**) Vertical polarization

Figure 8. Comparison simulation and measurement @ f_0 = 1.325 GHz: co-polar patterns. Normal array. Uniform amplitude and phase distribution.

The co-polar and cross-polar patterns for $\varphi = 90°$ are depicted in Figure 9. The measured cross-polarization suppression, 23 dB and 28 dB for the horizontal and vertical polarization, respectively, is lower than the simulated data. This difference can be certainly due to different reasons, especially the accuracy of the measurement, since the cross-polarization values are mainly below -20 dB, which leads to an extremely sensitive measurement. Other aspects such as the fabrication and manufacturing tolerances should also be considered. Nevertheless, it can be seen that the measured patterns meet the expected results very well.
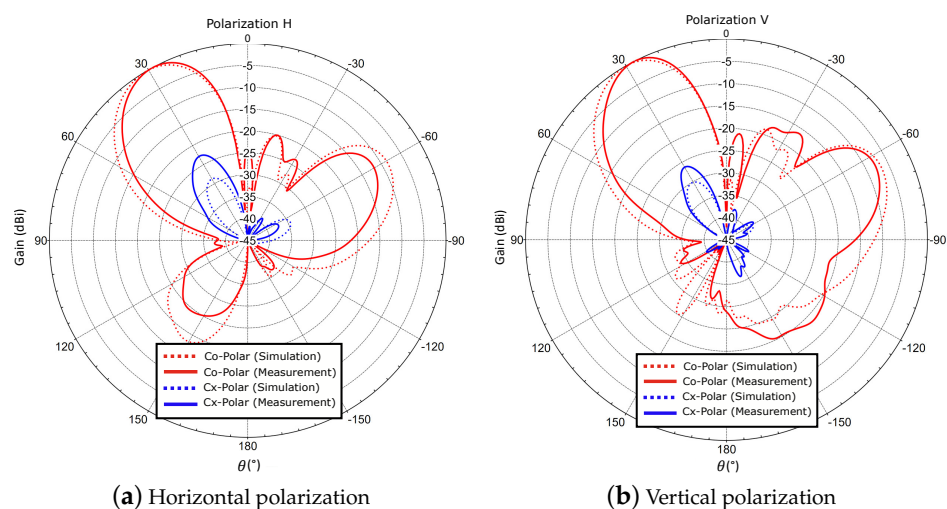
4.1.2. Beamforming

In this case, a potential application for SAR side-looking configuration is considered. In order to achieve an antenna main beam pointing at $\theta = 30°$, a phase difference of 120° among the antenna elements is applied. In addition, a triangular amplitude distribution is used to reduce the side lobe level and to yield a minimum at nadir ($\theta = 0°$), a direction that corresponds to the flight path projection. Table 3 shows the amplitude and phase values of each feeding port.

The desired symmetrical triangular amplitude tapering is implemented by means of 3 dB and 10 dB attenuators. The phase distribution is achieved with self-manufactured cables with the required electrical length. The simulated gain values are 10.6 dB and 11.9 dB for the horizontal and vertical polarization, respectively, which does not entirely meet the measured gain, since the amplitude tapering by means of the power divider and the attenuators are not considered in the calibration. The normalized co-polar and cross-polar patters for both polarizations are shown in Figure 10. As experienced in the measurements of the broadside array, the measured cross-polarization level is higher than the predicted values. The measured cross-polar suppression at the antenna main beam for the horizontal and vertical polarization is 23 dB and 26 dB, respectively.

(**a**) Horizontal polarization   (**b**) Vertical polarization

Figure 9. Comparison simulation and measurement @ f_0 = 1.325 GHz: co-polar & cross-polar patterns ($\varphi = 90°$). Normal array. Uniform amplitude and phase distribution.

(**a**) Horizontal polarization   (**b**) Vertical polarization

Figure 10. Comparison simulation and measurement @ f_0 = 1.325 GHz: normalized co-polar & cross-polar patterns ($\varphi = 90°$). Normal array. Beamforming.

Table 3. Amplitude tapering and phase distribution. Beamforming. Normal array.

Port H	Amplitude	Phase	Port V	Amplitude	Phase
H_1	−10 dB	0°	V_1	−10 dB	0°
H_2	−3 dB	120°	V_2	−3 dB	120°
H_3	0 dB	240°	V_3	0 dB	240°
H_4	−3 dB	0°	V_4	−3 dB	0°
H_5	−10 dB	120°	V_5	−10 dB	120°

4.2. Array with 180° Rotation of the Antenna Elements

In this configuration, a 180° sequential rotation of the array elements that involves the rotation of antennas 2 and 4 is performed, as it can be seen in Figure 11. This approach involves the out-of-phase feeding of the rotated elements. This feeding arrangement can lead to a suppression or reduction of the cross-polarized fields due to the phase inversion, while maintaining the same co-polarization pattern [20]. It can be noted in Figure 11 that, despite the 180° rotation of the array elements 2 and 4, the same geometrical slots as the previous configuration are involved in order to excite each polarization.

(**a**) Manufactured array

(**b**) Geometrical arrangement of the feeding slots.
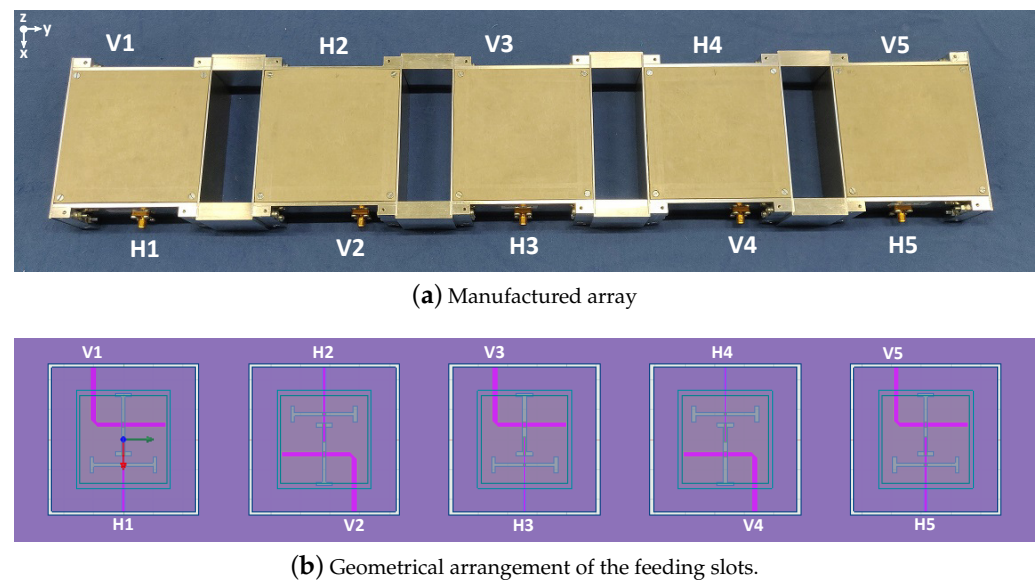
**Figure 11.** Manufactured array performing a 180° rotation of antenna elements 2 and 4.

4.2.1. Uniform Amplitude and Phase Distribution

The geometrical arrangement of the linear array with the 180° rotation of the antenna elements 2 and 4 is depicted in Figure 11. The amplitude and phase values of each antenna feeding port in order to achieve a broadside radiation are listed in Table 4. It can be noticed that the ports of the rotated elements H_2, V_2, H_4, V_4 are fed out-of-phase. In order to provide the inversion feeding, these elements are fed by means of cables with a length of half the guided wavelength regarding the cable lengths that feed the other antenna ports.

Table 4. Amplitude and phase values. Uniform. Array with 180° rotation.

Port H	Amplitude	Phase	Port V	Amplitude	Phase
H_1	0 dB	0°	V_1	0 dB	0°
H_2	0 dB	180°	V_2	0 dB	180°
H_3	0 dB	0°	V_3	0 dB	0°
H_4	0 dB	180°	V_4	0 dB	180°
H_5	0 dB	0°	V_5	0 dB	0°

A comparison of this configuration with the normal array in terms of co-polar and cross-polar patterns is shown in Figure 12. The measured co-polar patterns of the array with the 180° rotation are really similar to the measured patterns of the normal array. The measured cross-polarization, especially for the horizontal polarization, is higher than the simulated value. The overall cross-polarization performance of this configuration is comparable to the normal array, but it presents a higher sidelobe level. The cross-polarization suppression for both configurations are alike.
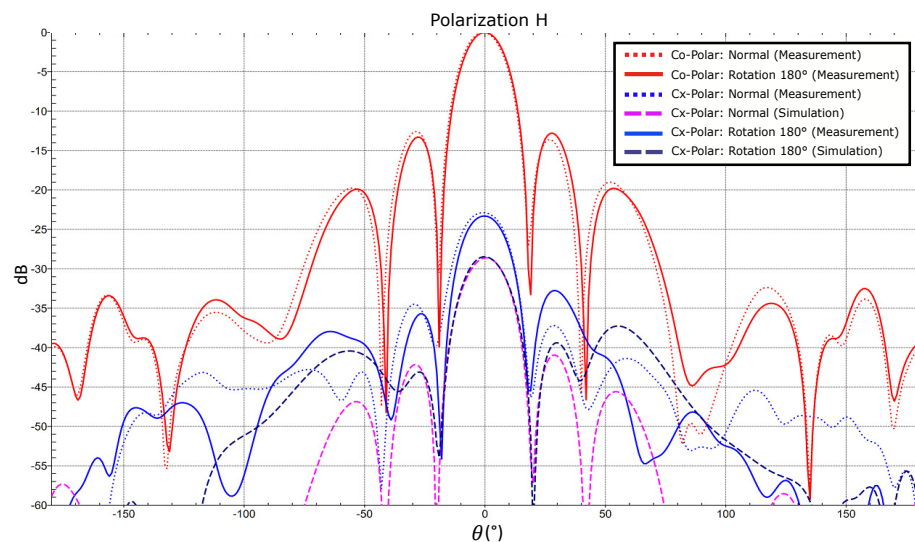
(**a**) Horizontal polarization
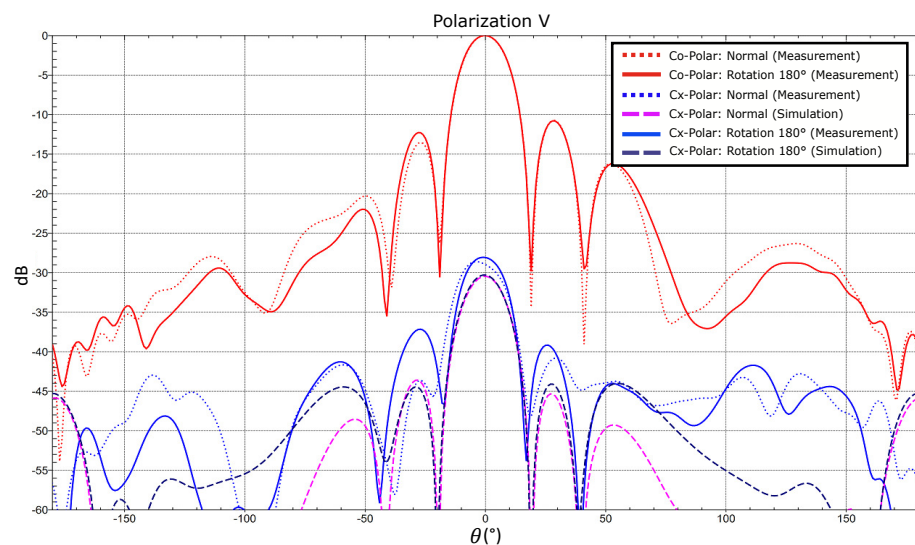
(**b**) Vertical polarization

Figure 12. Comparison normal array and array with 180° rotation @ f_0 = 1.325 GHz: normalized co-polar and cross-polar patterns ($\varphi = 90°$). Uniform amplitude and phase distribution.
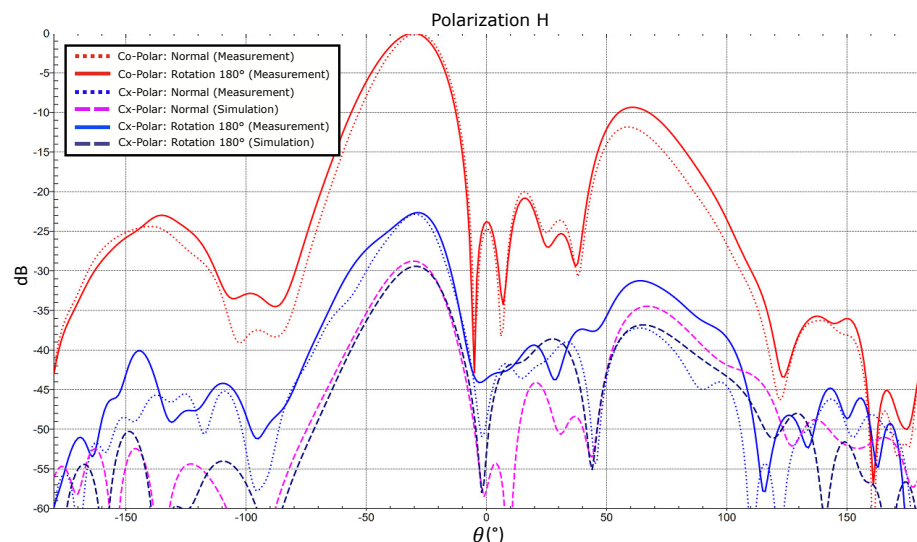
4.2.2. Beamforming

For this case, the same triangular amplitude tapering and phase values are used as in the previous configuration but considering the inversion phase feeding for the elements 2 and 4. The measured results and a comparison with the configuration of the normal array are shown in Figure 13.

As the uniform case, the measurement of the co-polar patterns for both configurations and polarizations agree very well. The measured cross-polarization values is again comparable for both configurations with a slight deterioration when the elements are rotated 180°,

providing an increase of the sidelobe level. The measured cross-polarization levels are higher than the simulated values. This difference is again more visible for the horizontal polarization. However, it can be seen that the overall measurements fit very well the simulated data.

In the view of the measurements results, it can be stated that the 180° rotation of the antenna elements 2 and 4 do not lead to any improvement in the cross-polarization level in comparison with the configuration of the normal array, since it provides similar cross-polarization suppression values.

(**a**) Horizontal polarization
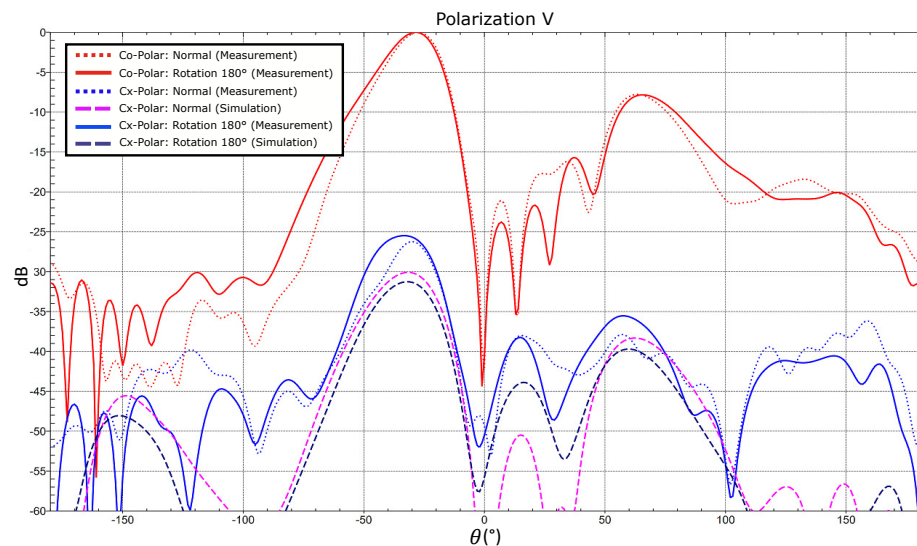
(**b**) Vertical polarization

Figure 13. Comparison normal array and array with 180° rotation @ f_0 = 1.325 GHz: normalized co-polar & cross-polar patterns ($\varphi = 90°$). Beamforming.
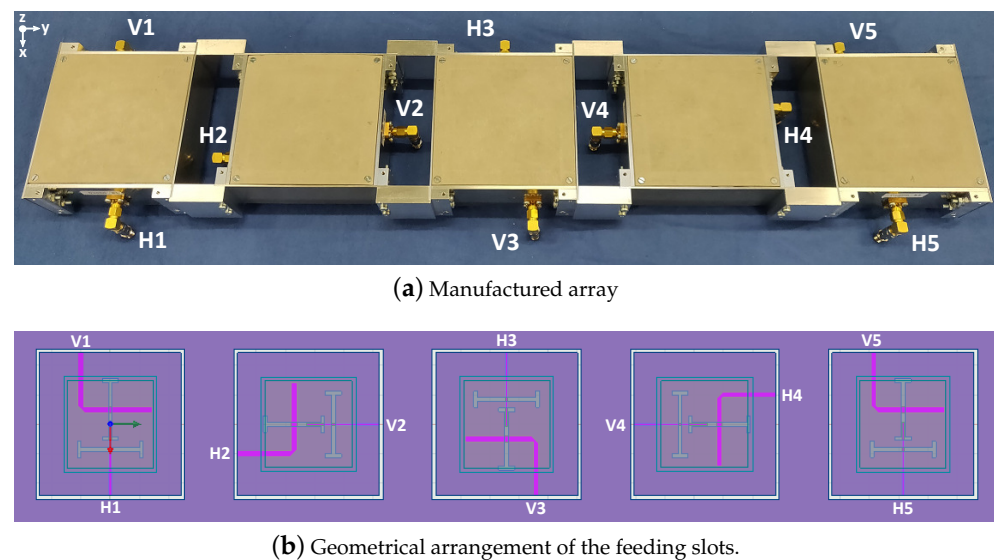
4.3. Array with Sequential 90° Rotation of the Antenna Elements

In this third configuration, a novel sequential 90° rotation approach of the array elements is performed. This leads to an element rotation topology where the antenna elements 2, 3 and 4 are respectively 90°, 180° and 270° rotated, while the elements 1 and 5 remain unchanged. The manufactured array is shown in Figure 14.

The geometrical 90° rotation involves an exchange of the polarization excitation of the antenna elements 2 and 4. This has to be considered, since, for a given array polarization,

different slot arrangements of the antenna elements are used. Electrically, this leads to a different feeding phase from which each antenna is fed, since the coupling slot involved in the antenna elements 1, 3, 5 and 2, 4 is not the same, with each slot being excited by means of microstrip lines with unequal electrical lengths, since they are placed on different substrate heights (Figure 2). Thus, a phase addition has to be applied in order to compensate such electrical length variation of the microstrip lines that feed the slots. The resulting geometrical arrangement of the feeding slots can be seen in Figure 14.

(**a**) Manufactured array

(**b**) Geometrical arrangement of the feeding slots.

Figure 14. Sequential 90° rotation of the antenna elements.

According to the values of Table 2, lines 1 and lines 2 have a length l_1 and l_2 of 25.95 mm and 52.3 mm, respectively. As each microstrip line is placed on different FR4 substrate heights h_{feed1} and h_{feed2}, its guided wavelengths are $\lambda_1 = 113$ mm and $\lambda_2 = 128$ mm. Each slot is fed with a phase given by the electrical length of the line from which it is coupled. The electrical lengths l_1 and l_2 lead to a phase shifting at slot 1 and slot 2, respectively φ_1 and φ_2, given by:

$$\varphi_1 = (l_1/\lambda_1) * 2\pi = 83° \tag{1}$$

$$\varphi_2 = (l_2/\lambda_2) * 2\pi = 147° \tag{2}$$

That leads to a feeding phase difference between both lines of:

$$\Delta\varphi = \varphi_2 - \varphi_1 \approx 70° \tag{3}$$

The exact phase value is rounded several degrees as simulations show that the precise phase value from which each slot is fed is slightly influenced by the offset of the slot 1, and the position of the slot 2 that is placed above the end of the line 1. This phase difference $\Delta\varphi$ has to be compensated when exciting the same polarization by means of different feeding slot arrangements.

In addition, this sequential rotation approach leads to a 180° rotation of the antenna element 3, as it can be seen in Figure 14, just like it was presented in the previous configuration. This requires an inversion phase feeding of the ports H_3, V_3, since they have to be fed out of phase.

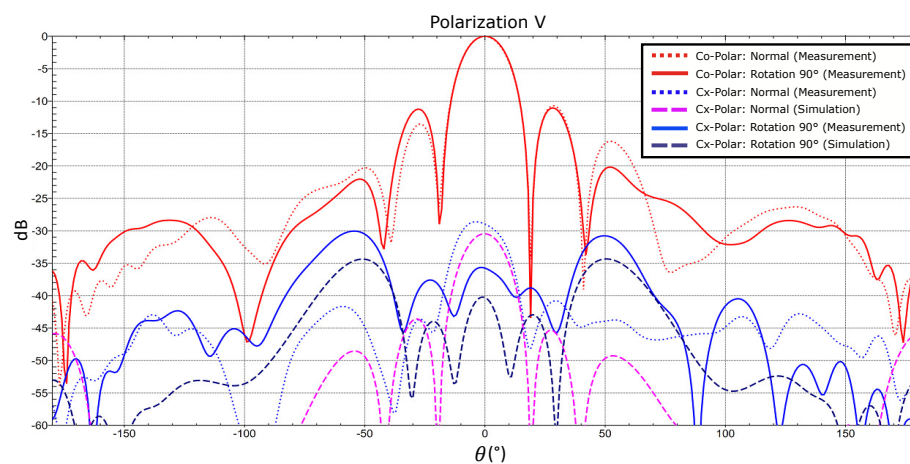### 4.3.1. Uniform Amplitude and Phase Distribution

The aforementioned design considerations lead to the amplitude and phase values for each antenna feeding port listed in Table 5.

A comparison between the normal array and the array with the sequential 90° rotation of the antenna elements, when applying uniform amplitude and phase, is depicted in

Figure 15. It can be seen that both configurations provide the same co-polar pattern with broadside radiation, with slight differences regarding the side lobe level of the vertical polarization. The measured cross-polarization is again higher than the simulation, as it is experienced in the previous measurements. However, it can be stated that the cross-polarization performance of the array with the sequential 90° rotation is considerably enhanced within the main beam with the penalty of increasing it in the ranges $\theta \pm 50°$ but far beyond the antenna main beam. The measured improvement at $\theta = 0°$ is almost 10 dB and 8 dB for the horizontal and vertical polarization, thus achieving a measured cross-polarization suppressions of 32 dB and 36 dB, respectively, which still remain below the simulated values. This slightly difference can be expected, since the measured range of the cross-polarization values are relatively low in the logarithmic scale, leading to an extremely sensitive measurement. It has to be also considered that the antenna elements are not exactly identically constructed due to fabrication tolerances and manufacturing processes. It can be also seen that the measured cross-polarization patterns agree with the predicted simulation data.
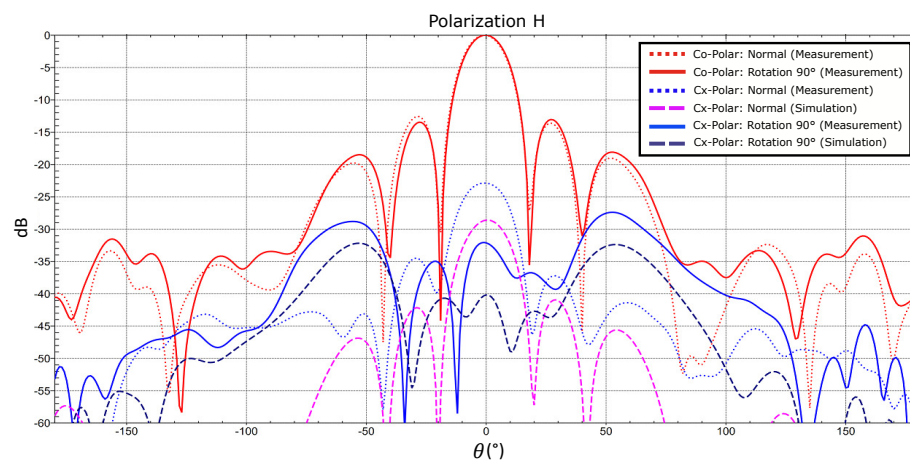
(**a**) Horizontal polarization.

(**b**) Vertical polarization.

Figure 15. Comparison normal array and array with sequential 90° rotation @ f_0 = 1.325 GHz: normalized co-polar & cross-polar patterns ($\varphi = 90°$). Uniform amplitude and phase distribution.
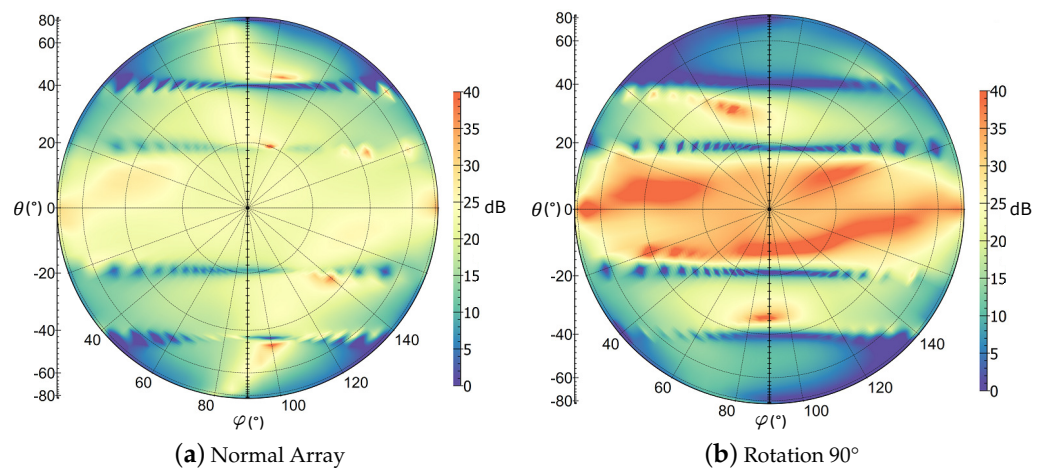
Table 5. Amplitude and phase values. Uniform amplitude and phase distribution. Array with sequential 90° rotation.

Port H	Amplitude	Phase	Port V	Amplitude	Phase
H_1	0 dB	0°	V_1	0 dB	0°
H_2	0 dB	70°	V_2	0 dB	110°
H_3	0 dB	180°	V_3	0 dB	180°
H_4	0 dB	250°	V_4	0 dB	−70°
H_5	0 dB	0°	V_5	0 dB	0°

A comparison in terms of cross-polarization suppression of the normal array and the array with the sequential 90° rotation of the antenna elements is shown in Table 6. A polar representation of the cross-polarization suppression values is depicted in Figure 16. It can be seen that with the sequential 90° rotation, a great improvement regarding the cross-polar suppression within the antenna main beam is achieved.

Table 6. Comparison of the cross-polarization suppression @ f_0 = 1.325 GHz. Uniform amplitude and phase distribution.

	Polarization H		Polarization V	
	Simulation	**Measurement**	**Simulation**	**Measurement**
Normal Array	28.6 dB	22.87 dB	30.46 dB	28.1 dB
Rotation 90°	40.17 dB	32.15 dB	40.28 dB	35.72 dB

(**a**) Normal Array   (**b**) Rotation 90°

Figure 16. Measured cross-polar suppression @ f_0 = 1.325 GHz. Uniform amplitude and phase distribution. Horizontal polarization.
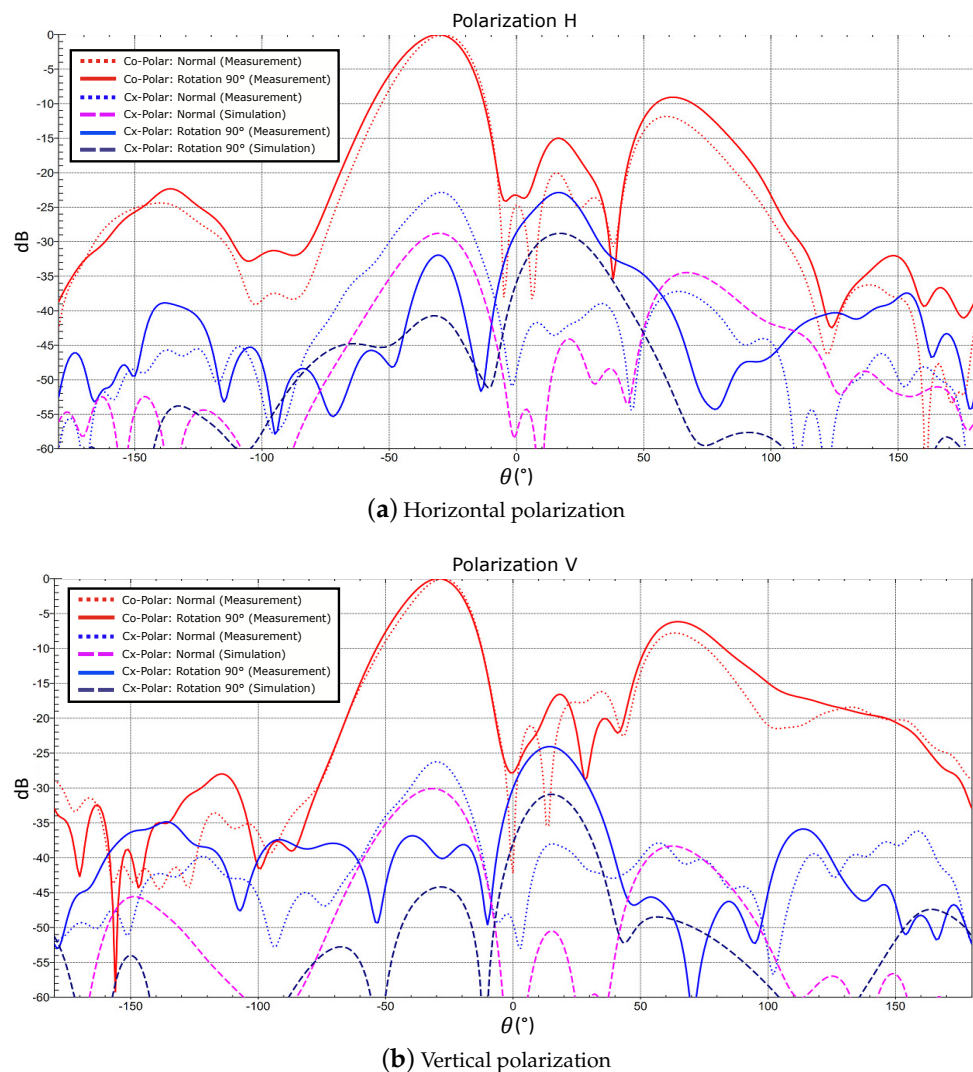
4.3.2. Beamforming

For the case of side-looking, the amplitude tapering and phase distribution values are given by Table 7.

Table 7. Amplitude and phase values. Beamforming. Array with sequential 90° rotation.

Port H	Amplitude	Phase	Port V	Amplitude	Phase
H_1	−10 dB	0°	V_1	−10 dB	0°
H_2	−3 dB	70° + 120°	V_2	−3 dB	110° + 120°
H_3	0 dB	180° + 240°	V_3	0 dB	180° + 240°
H_4	−3 dB	250°	V_4	−3 dB	−70°
H_5	−10 dB	0° + 120°	V_5	−10 dB	0° + 120°

The performance of this configuration is compared with the normal array in Figure 17 when beamforming is applied. Both array configurations provide a similar co-polar patterns, as expected. Despite the fact that the measured cross-polar level for the horizontal polarization at the antenna main beam direction $\theta = 30°$ is higher than the simulated value, it remains 10 dB below the measured value for the normal array. The measurement of the vertical polarization shows an improvement of almost 14 dB in comparison with the normal array, achieving a cross-polarization suppression of 40 dB. The sequential 90° rotation of the antenna elements also provides a shift of the cross-polarization maximum beyond the antenna main beam. The overall measured cross-pol pattern meets the simulated data, which demonstrates the improvement of the cross-polarization performance by means of the presented 90° rotation approach. An overview in terms of the cross-polarization suppression values of this configuration and the normal array, when applying beamforming, is shown in Table 8 and Figure 18. The polar plot provides an additional angular representation, where the improvement achieved in the antenna main beam direction is clearly seen, especially all over the direction $\varphi = 90°$. A more symmetric cross-polarization pattern is also achieved, with a deterioration in the angular range $\theta > 0°$, far beyond the direction of the main radiation.


(**a**) Horizontal polarization

(**b**) Vertical polarization

Figure 17. Comparison normal array and array with sequential 90° rotation @ f_0 = 1.325 GHz: normalized co-polar & cross-polar patterns ($\varphi = 90°$). Beamforming.

Table 8. Comparison of cross-polarization suppression @ f_0 = 1.325 GHz. Beamforming.

	Polarization H		Polarization V	
	Simulation	**Measurement**	**Simulation**	**Measurement**
Normal Array	28.75 dB	22.82 dB	30.14 dB	26.04 dB
Rotation 90°	40.85 dB	31.95 dB	44.23 dB	39.71 dB

(**a**) Normal Array (**b**) Rotation 90°
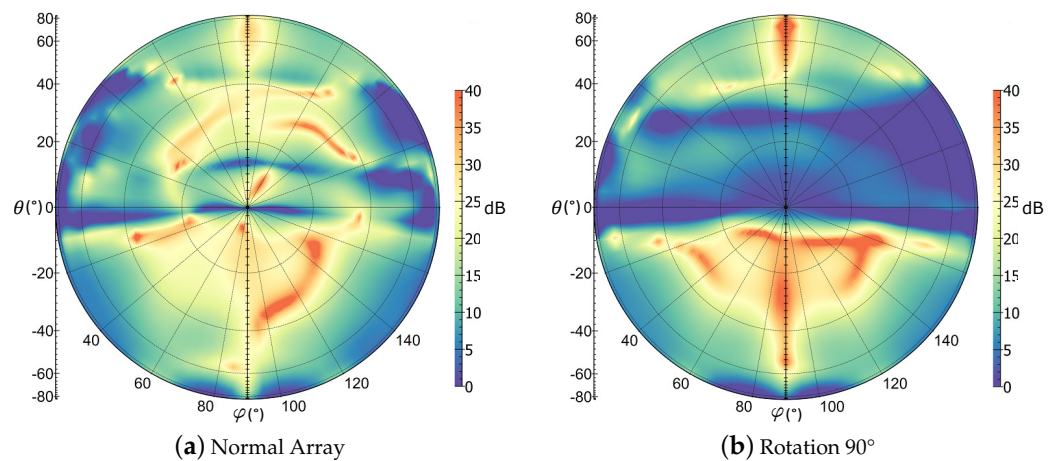
Figure 18. Measured cross-polar suppression @ f_0 = 1.325 GHz. Beamforming. Vertical polarization.

5. Discussion

A comparison of this work with some of the given references in terms of cross-polarization performance is shown in Table 9. This comparison provides an overview of the state-of-the-art, since, for each of the listed works, different electrical parameters such as antenna geometries, feeding configurations, and array topologies are involved. The presented work is the only one that performs a rotation topology in linear arrays, as the other works are based on the decomposition of planar arrays into subarrays.

In order to provide a fairer comparison, the proposed sequential 90° rotation topology is extended to the case of a planar array of 5 × 5 elements where the rotation approach is applied along the two antenna axes. The simulated results are also included in the comparison.

Table 9. Comparison cross-polarization performance of the proposed work with some of the given references.

Ref.	Frequency Band	Array Topology	Antenna Unit	Cross-Polar Suppression
[18]	L-Band	8 × 2	Probe-fed patch	38 dB
[19]	L-Band	8 × 2	Probe-fed stacked patch	39 dB
[20]	S-Band	6 × 6	Hybrid-fed patch	36 dB
[21]	S-Band	12 × 12	Aperture coupled stacked patch	30 dB
[23]	X-Band	20 × 20	Orthogonal set of dipoles	40 dB (simulated)
[24]	X-Band	8 × 8	Single-polarized probe-fed U-Slot	Improvement 20 dB
This work	L-Band	5 × 1	Cavity-box aperture coupled stacked patch	39.7 dB
Extension of this work	L-Band	5 × 5	Cavity-box aperture coupled stacked patch	53.8 dB (simulated)

6. Conclusions

In this manuscript, a novel sequential 90° rotation approach of the antenna elements in a linear array designed for airborne SAR applications is presented. This rotation topology leads to improvements in the cross-polarization level within the antenna main beam in

comparison with the standard array configuration of up to 14 dB. Measured values show a cross-polarization suppression of almost 40 dB. The validation of this rotation approach is confirmed by considering uniform phase and amplitude distribution and beamforming with amplitude tapering. Despite the fact that the measurements match the simulated values really well, the required accuracy and sensitivity of cross-polarization measurements make a demanding task to achieve cross-polarization suppression values better than 40 dB, as it is accomplished in the simulation.

To the best of author's knowledge, no similar sequential 90° rotation approach has been implemented in dual polarized linear array applications. This technique can be extended to planar arrays, achieving higher cross-polarization suppression values. The findings of the proposed work are expected to be applied in the design of the new L-Band antenna for the next generation airborne SAR system of the German Aerospace Center (DLR).

Author Contributions: Conceptualization, D.L., M.L., H.E. and V.E.B.; methodology, D.L., M.L., H.E. and V.E.B.; software, D.L., M.L. and B.G.; validation, D.L. and B.G.; formal analysis, D.L.; investigation, D.L.; resources, D.L., M.L. and B.G.; data curation, D.L. and B.G.; writing—original draft preparation, D.L.; writing—review and editing, D.L.; visualization, D.L.; supervision, M.L., H.E. and V.E.B.; project administration, M.L.; funding acquisition, M.L. All authors have read and agreed to the published version of the manuscript.

References

1. Ban Y.; Jacob A.; Gamba P. Spaceborne SAR data for global urban mapping at 30 m resolution using a robust urban extractor. *ISPRS J. Photogramm. Remote Sens.* **2015**, *103*, 28–37. [CrossRef]
2. Cerutti-Maori, D.; Klare, J.; Brenner, A.R.; Ender, J.G. Wide Area Traffic Monitoring with the SAR/GMTI System PAMIR. *Trans. Geosci. Remote Sens.* **2008**, *46*, 3019–3030. [CrossRef]
3. Brusch, S.; Lehner, S.; Fritz, T.; Soccorsi, M.; Soloviev, A.; van Schie, B. Ship Surveillance with TerraSAR-X. *Trans. Geosci. Remote Sens.* **2011**, *49*, 1092–1103. [CrossRef]
4. Almeida-Filho, R.; Rosenqvist, A.; Shimabukuro, Y.E.; Silva-Gomez, R. Detecting deforestation with multitemporal L-band SAR imagery:a case study in western Brazilian Amazonia. *Int. J. Remote Sens.* **2006**, *28*, 1383–1390. [CrossRef]
5. Limbach, M.; Gabler, B.; Horn, R.; Kość, A.; Di Maria, A.; Scheiber, R. P-band antenna array for airborne SAR application and DBF SAR demonstration. In Proceedings of the 2015 9th European Conference on Antennas and Propagation (EuCAP), Lisbon, Portugal, 13–17 April 2015; pp. 1–5.
6. Lorente, D.; Limbach, M.; Gabler, B. L-Band Antenna Array for Next, Generation DLR Airborne SAR Sensor. In Proceedings of the 2019 12th German Microwave Conference (GeMiC), Stuttgart, Germany, 25–27 March 2019; pp. 182–185.
7. IEEE Standard Letter Designations for Radar-Frequency Bands. Available online: https://ieeexplore.ieee.org/stamp/stamp.jsp?arnumber=29086 (accessed on 30 March 2021).
8. Huang, Y.; Zhang, Q.; Ferro-Famil, L. Forest Height Estimation Using a Single-Pass Airborne L-Band Polarimetric and Interferometric SAR System and Tomographic Techniques. *Remote Sens.* **2021**, *13*, 487. [CrossRef]
9. Merzouki, A.; McNairn, H.; Powers, J.; Friesen, M. Synthetic Aperture Radar (SAR) Compact Polarimetry for Soil Moisture Retrieval. *Remote Sens.* **2019**, *11*, 2227. [CrossRef]
10. Martone, M.; Rizzoli, P.; Wecklich, C.; González, C.; Bueso-Bello, J.L.; Valdo, P.; Schulze, D.; Zink, M.; Krieger, G.; Moreira, A. The global forest/non-forest map from TanDEM-X interferometric SAR data. *Remote Sens. Environ.* **2018**, *205*, 352–373. [CrossRef]
11. Reigber, A.; Schreiber, E.; Trappschuh, K.; Pasch, S.; Müller, G.; Kirchner, D.; Geßwein, D.; Schewe, S.; Nottensteiner, A.; Limbach, M.; et al. The High-Resolution Digital-Beamforming Airborne SAR System DBFSAR. *Remote Sens.* **2020**, *12*, 1710. [CrossRef]
12. Horn, R.; Nottensteiner, A.; Reigber, A.; Fischer, J.; Scheiber, R. F-SAR—DLR's new multifrequency polarimetric airborne SAR. In Proceedings of the 2009 IEEE International Geoscience and Remote Sensing Symposium, Cape Town, South Africa, 12–17 July 2009; pp. 902–905.

13. Huber. S.; de Almeida, F.Q.; Villano, M.; Younis, M.; Krieger, G.; Moreira, A. Tandem-L: A Technical Perspective on Future Spaceborne SAR Sensors for Earth Observation. *IEEE Trans. Geosci. Remote Sens.* **2018**, *56*, 4792–4807. [CrossRef]

14. Kość, A.; Di Maria, A.; Limbach, M.; Horn, R.; Reigber, A. A 5 way lumped-elements Wilkinson power divider. In Proceedings of the 2013 7th European Conference on Antennas and Propagation (EuCAP), Gothenburg, Sweden, 8–12 April 2013; pp. 357–360.

15. Lorente, D.; Schreiber, A.; Limbach, M.; Esteban, H.; Boria, V.E. High Permittivity CPW-SIW Power Divider for Antenna Feed Networks in Airborne Phased Arrays Applications. In Proceedings of the 2020 17th European Radar Conference (EuRAD), Utrecht, The Netherlands, 10–15 January 2021; pp. 254–257.

16. Limbach, M.; Di Maria, A.; Reigber, A.; Gabler, B.; Horn, R.; Kosc, A. S-Band Antenna for Airborne Polarimetric and Interferometric SAR-Applications. In Proceedings of the 2013 7th European Conference on Antennas and Propagation (EuCAP), Gothenburg, Sweden, 8–12 April 2013; pp. 2968–2972.

17. Di Maria, A.; Limbach, M.; Horn, R.; Reigber, A. Design and Measurements of a C-Band Array for High Power High Bandwidth SAR Application. In Proceedings of the 2013 7th European Conference on Antennas and Propagation (EuCAP), Gothenburg, Sweden, 8–12 April 2013; pp. 1803–1806.

18. Woelders, K.; Granholm, J. Cross-Polarization and Sidelobe Suppressionin Dual Linear Polarization Antenna Arrays. *IEEE Trans. Antennas Propag.* **1997**, *45*, 1727–1740. [CrossRef]

19. Granholm, J.; Woelders, K. Dual polarization stacked microstrip patch antenna array with very low cross-polarization. *IEEE Trans. Antennas Propag.* **2001**, *49*, 1393–1402. [CrossRef]

20. Saeidi-Manesh, H.; Zhang, G. High-Isolation, Low Cross-Polarization, Dual-Polarization, Hybrid Feed Microstrip Patch Array Antenna for MPAR Application. *IEEE Trans. Antennas Propag.* **2018**, *66*, 2326–2332. [CrossRef]

21. Saeidi-Manesh, H.; Karimkashi, S.; Zhang, G.; Doviak, R. High-Isolation Low Cross-polarization Phased-Array Antenna for MPAR Application. *Radio Sci.* **2017**, *52*, 1544–1557. [CrossRef]

22. Saeidi-Manesh, H.; Zhang, G. Challenges and Limitations of the Cross-Polarization Suppression in Dual-Polarization Antenna Arrays Using Identical Subarrays. *IEEE Trans. Antennas Propag.* **2019**, *68*, 2853–2866. [CrossRef]

23. Florencio, R.; Encinar, J.A.; Boix, R.R.; Pérez-Palomino, G.; Toso, G. Cross-polar reduction in reflectarray antennas by means of element rotation. In Proceedings of the 2016 10th European Conference on Antennas and Propagation (EuCAP), Davos, Switzerland, 10–15 April 2016.

24. Yin, W.; Liang, X.; Chen, A.; Zhang, Z.; Shi, L.; Guan, F.; Liu, X.; Zi, J. Cross-polarization suppression for patch array antennas via generalized Kerker effects. *Opt. Express* **2020**, *28*, 40–47. [CrossRef]

25. Fan, F.; Yan, Z.; Xu, P.; Tan, K. Sequential Rotation Feeds Microstrip Array. *Microwaves&RF* **2013**, *52*, 55–58.

26. Greda, L.K.; Dreher, A. Tx-terminal phased array for satellite communication at Ka-band. In Proceedings of the 2007 European Microwave Conference, Munich, Germany, 9–12 October 2007.

27. Hu, W.; Wen, G.; Inserra, D.; Huang, Y.; Li, J.; Chen, Z. A Circularly Polarized Antenna Array with Gain Enhancement for Long-Range UHF RFID Systems. *Electronics* **2019**, *8*, 400. [CrossRef]

28. Baggen, L.; Holzwarth, S.; Simon, W.; Litzsche, O. Phased array using the sequential rotation principle: Analysis of coupling effects. In Proceedings of the IEEE International Symposium on Phased Array Systems and Technology 2003, Boston, MA, USA, 14–17 October 2003.

29. Deng, C.; Li, Y.; Zhang, Z.; Feng, Z. A Wideband Sequential-Phase Fed Circularly Polarized Patch Array. *IEEE Trans. Antennas Propag.* **2014**, *62*, 3890–3893. [CrossRef]

30. Garcia-Garcia, Q. Linear arrays of sequentially rotated circularly polarized patch radiators. *Microw. Opt. Technol. Lett.* **2000**, *25*, 387–390. [CrossRef]

31. Garcia-Garcia, Q. Scanning properties of sequential rotated linear arrays of circularly polarized patch. *Microw. Opt. Technol. Lett.* **2001**, *30*, 343–350. [CrossRef]

32. Pozar, D.M. Microstrip Antennas. *Proc. IEEE* **1992**, *80*, 79–91. [CrossRef]

33. Pozar, D.M. A Review of Aperture Coupled Microstrip Antennas: History, Operation, Development, and Applications. 1996. Available online: http://www.ecs.umass.edu/ece/pozar/aperture.pdf (accessed on 7 April 2021).

34. Rowe, W.S.T.; Waterhouse, R.B. Investigation into the performance of proximity coupled stacked patches. *IEEE Trans. Antennas Propag.* **2006**, *54*, 1693–1698. [CrossRef]

35. Bugaj, M.; Wnuk, M. Bandwidth Optimization of Aperture-Coupled Stacked Patch Antenna. In *Advancement in Microstrip Antennas with Recent Applications*; Kishk, A., Ed.; IntechOpen: London, UK, 2013.

36. Pozar, D.M.; Targonski, S.D. Improved coupling for aperture coupled microstrip antenna. *IEEE Electron Device Lett.* **1991**, *27*, 1129–1131. [CrossRef]

37. Limbach, M.; Gabler, B.; Di Maria, A.; Horn, R.; Reigber, A. DLR Compact Test Range facility. In Proceedings of the 2012 6th European Conference on Antennas and Propagation (EuCAP), Prague, Czech Republic, 26–30 March 2012; pp. 1276–1280.

38. Mini-Circuits 6 Way Power Splitter/Combiner ZB6PD-17-S Data Sheet. Available online: https://www.minicircuits.com/pdfs/ZB6PD-17-S.pdf (accessed on 30 March 2021).